Spin-polarized low-energy (e, 2e) spectroscopy of non-magnetic surfaces

1999 J. Phys.: Condens. Matter 11 9555

(http://iopscience.iop.org/0953-8984/11/48/313)

J. Phys.: Condens. Matter **11** (1999) 9555–9570. Printed in the UK PII: S0953-8984(99)05863-4

Spin-polarized low-energy (e, 2e) spectroscopy of non-magnetic surfaces

H Gollisch, Xiao Yi†, T Scheunemann and R Feder
Theoretische Festkörperphysik, Universität Duisburg, D-47048 Duisburg, Germany

Received 9 July 1999, in final form 12 October 1999

Abstract. For spin-polarized low-energy electrons impinging on non-magnetic crystalline surfaces, the collision with a valence electron and the ensuing emission of an electron pair are treated in a distorted-wave Born approximation formalism with exchange, in which the four relevant quasi-one-electron states are solutions of the Dirac equation. Numerical calculations for W(001), which were carried out in two coplanar geometries with normal and grazing incidence of a primary beam polarized normal to the reaction plane, show that the (e, 2e) cross section changes significantly upon reversal of the polarization. Originating mainly from spin–orbit coupling in the valence electron state, asymmetries of up to 30% occur in conjunction with sizable intensity. The calculated spectra respond sensitively to changes in the surface structure.

(Some figures in this article appear in colour in the electronic version; see `www.iop.org`)

1. Introduction

For electrons impinging on atomic or solid targets, an important reaction channel involves a single collision event with a valence electron resulting in two electrons leaving the solid. Energy- and momentum-resolved observation of these two electrons is frequently referred to as (e, 2e) spectroscopy. A variety of recent results and ample references to a vast body of literature may e.g. be found in the monograph [1]. (e, 2e) spectroscopy applied to solids in the transmission mode using high-energy primary electrons is a well-established technique, which in particular reveals the momentum density of the valence electrons (cf. e.g. [2, 3]).

At low primary electron energies (less than a few 100 eV), the short mean free paths necessitate the observation of the electron pair in the reflection mode for solid surfaces. Substantial experimental and theoretical progress was only made fairly recently (see [4–12] and references therein).

In particular, an extensive joint experimental and theoretical study of the energy- and angle-resolved (e, 2e) cross section was recently carried out for primary electrons with energies below 25 eV incident on a clean W(001) surface [9]. A time-of-flight technique made it possible to measure simultaneously energies and momenta of two electrons emerging in coincidence. In the theoretical treatment, elastic multiple scattering by the ion cores was fully taken into account for the primary electron, the valence electron, and the two detected electrons. The good overall agreement which was reached between experimental data and their calculated counterparts inspired confidence in the methods used and gave insight into details of the (e, 2e) process.

† Permanent address: Physics Department, Huazhong University of Science and Technology, Wuhan, China.

0953-8984/99/489555+16$30.00

In the above low-energy (e, 2e) studies for solid surfaces, the primary electron beam was unpolarized and the two outgoing electrons were not spin analysed. Even for non-magnetic surfaces, however, one can expect a dependence of the (e, 2e) cross section on the spin polarization of the primary beam: on the one hand, such spin asymmetry is well known from low-energy electron diffraction (LEED) (see e.g. [13–15] and references therein), and on the other hand, in (e, 2e) studies the primary electron state is a LEED state and the outgoing ones are time-reversed LEED states (cf. [9]). The physical origin of this asymmetry is spin–orbit coupling (SOC). Furthermore, SOC effects are well known to be significant in the valence electron structure of bulk solids (cf. e.g. [16, 17]) and of surface systems (cf. e.g. [18, 19] and references therein). The valence electron state can therefore also be expected to give rise to an observable asymmetry of the (e, 2e) cross section.

It is the aim of the present work to explore the SOC-induced spin asymmetry of the (e, 2e) intensity for non-magnetic surfaces by means of calculations made on the basis of the spin-dependent extension of a method which has been demonstrated [9] to be quantitatively adequate for spin-averaged (e, 2e) studies. Insight into the collision mechanism and in particular into the relative importance of SOC in the four participating one-electron states is obtained by making additional calculations, in which SOC and elastic layer scattering matrix elements are selectively switched off.

This paper is organized as follows. The theoretical method and specific model assumptions for the numerical calculations are described in section 2. In section 3 we present and discuss calculated spin-dependent low-energy (e, 2e) results for W(001) for two coplanar scattering geometries.

2. Theory

2.1. Model and formalism

The (e, 2e) reaction cross section for spin-polarized low-energy electrons impinging on a non-magnetic crystalline surface system can be calculated by means of an extension of the method described in [9]. In what follows we outline this method and derive the appropriate spin-dependent expressions.

The observable quantity of interest is the cross section for the following (e, 2e) reaction. A primary electron, which at the source (electron gun) has kinetic energy E_1, momentum $\boldsymbol{k}_1$, and spin alignment $\sigma_1 = \pm$ with respect to some given axis $\boldsymbol{e}$, collides with a valence electron (with $E_2 < E_F$, where E_F is the Fermi energy), and two directly produced outgoing electrons are observed, which at the detectors have kinetic energies E_3 and E_4 and momenta $\boldsymbol{k}_3$ and $\boldsymbol{k}_4$. Let the spin of the two outgoing electrons not be resolved, since this is beyond present-day experimental capabilities. The energy E_2 of the valence electron is determined from the energies of the primary and the detected electrons by the conservation law $E_1 + E_2 = E_3 + E_4$. Because of lattice periodicity parallel to the surface, the surface-parallel momentum $\boldsymbol{k}_i^{\parallel}$ with $i = 1, 2, 3, 4$ is a good quantum number for each of the four electron states; $\boldsymbol{k}_1^{\parallel}$ and $\boldsymbol{k}_{3,4}^{\parallel}$ are given as the surface projections of the incident and the detected electron momenta, respectively, and $\boldsymbol{k}_2^{\parallel}$ is then determined by the conservation law $\boldsymbol{k}_1^{\parallel} + \boldsymbol{k}_2^{\parallel} = \boldsymbol{k}_3^{\parallel} + \boldsymbol{k}_4^{\parallel}$.

The four one-electron states are obtained as solutions of a Dirac equation with an effective one-electron potential describing the interaction with the atomic nuclei and the ground-state electrons of the surface system. For each electron state, there are consequently two independent spinor solutions $\psi_i^{\sigma_i}(\boldsymbol{x})$, which are characterized by the spin label $\sigma_i = \pm$. For the primary electron state, the spin-quantization axis and the spin label σ_1 are fixed by the boundary condition at the spin-polarized electron source.

The primary electron state $\psi_1^{\sigma_1}(\boldsymbol{x})$, which is the usual relativistic LEED state, and $\psi_3^{\sigma_3}$ and $\psi_4^{\sigma_4}$, which are time-reversed LEED states, are calculated by means of a relativistic layer KKR method (cf. [14]) with the appropriate boundary conditions. The valence electron states are obtained by matching—at the surface—linear combinations of bulk Bloch waves inside the crystal with exponentially decaying plane waves in the vacuum half-space. There are usually $2N$ independent solutions $\psi_2^{n\sigma_2}(\boldsymbol{x})$, where the index $n = 1, \ldots, N$ corresponds to the N outward-propagating bulk Bloch-wave pairs.

The reaction cross section is approximated in first-order perturbation theory in the form $|\langle 34|H_{ee}|12\rangle|^2$, where H_{ee} is the electron–electron interaction Hamiltonian, and $|12\rangle$ and $|34\rangle$ are antisymmetrized products of the above one-electron states. For primary electrons with spin orientation σ_1 relative to an axis $\boldsymbol{e}$ (i.e. spin-polarization vector $\boldsymbol{P}_1 = \sigma_1 \boldsymbol{e}$) and fixed energy and momentum, and for spin-unresolved detection of the outgoing electrons in fixed directions, this leads to the following expression for the (e, 2e) cross section ('intensity'):

$$I^{\sigma_1}(E_3, E_4) = (k_3 k_4 / k_1) \sum_{\sigma_3, \sigma_4} \sum_{E_2, \boldsymbol{k}_2^{\parallel}, n\sigma_2} |f_{1,2,3,4}^{\sigma_1, n\sigma_2, \sigma_3, \sigma_4} - g_{1,2,3,4}^{\sigma_1, n\sigma_2, \sigma_3, \sigma_4}|^2 \delta(E_1 + E_2 - E_3 - E_4) \times \delta(\boldsymbol{k}_1^{\parallel} + \boldsymbol{k}_2^{\parallel} - \boldsymbol{k}_3^{\parallel} - \boldsymbol{k}_4^{\parallel}) \tag{1}$$

where f and g are direct and exchange scattering amplitudes:

$$f_{1,2,3,4}^{\sigma_1, n\sigma_2, \sigma_3, \sigma_4} = \int \psi_3^{\sigma_3 *}(\boldsymbol{x}) \psi_4^{\sigma_4 *}(\boldsymbol{x}') V(\boldsymbol{x}, \boldsymbol{x}') \psi_1^{\sigma_1}(\boldsymbol{x}) \psi_2^{n\sigma_2}(\boldsymbol{x}') \, \mathrm{d}^3 x \, \mathrm{d}^3 x'. \tag{2}$$

The expression for g is the same except that $\boldsymbol{x}$ and $\boldsymbol{x}'$ are interchanged in the first product term. The state subscripts i implicitly contain the quantum numbers E_i and $k_i^{\parallel}$. Since the spin of the outgoing electrons is not resolved, the observed cross section is the σ_3, σ_4 sum over cross sections involving states $\psi_3^{\sigma_3}$ and $\psi_4^{\sigma_4}$. Each of these partial cross sections consists of a sum over the independent valence states. $V(\boldsymbol{x}, \boldsymbol{x}')$ in equation (2) approximates the electron–electron interaction H_{ee} by the Coulomb interaction statically screened by the ground-state electrons of the target:

$$V(\boldsymbol{x}, \boldsymbol{x}') = \int \mathrm{d}^3 x'' \, \varepsilon^{-1}(\boldsymbol{x}, \boldsymbol{x}'') / |\boldsymbol{x}'' - \boldsymbol{x}'| \tag{3}$$

where $\varepsilon(\boldsymbol{x}, \boldsymbol{x}'')$ is the dielectric function of the crystalline surface system.

The asymmetry A of the cross section upon reversal of the primary electron spin is defined from the intensities $I^{\pm}$ in equation (1) as

$$A(E_3, E_4) = (I^+ - I^-)/(I^+ + I^-). \tag{4}$$

If, for a non-magnetic target system, spin–orbit coupling is absent in all four states, the spinor wave functions $\psi_i^{\sigma_i}(\boldsymbol{x})$ reduce to products of a scalar spatial wave function with a basic spinor, and one easily obtains from equations (1), (2) that $I^+ = I^-$ and therefore $A = 0$. SOC—in at least one of the participating one-electron states—is thus essential for the (e, 2e) cross section to depend on the primary electron spin.

2.2. Switch-off modifications

In the above formalism, the four one-electron states $\psi_i^{\sigma_i}(\boldsymbol{x})$ contain elastic multiple scattering from the ion-core lattice and, being solutions of the Dirac equation, spin–orbit coupling. To obtain detailed insight into the physical origin of individual features of the intensities $I^{\pm}$ and the asymmetry A associated with them, we find it useful to perform additional calculations, in which the individual $\psi_i^{\sigma_i}(\boldsymbol{x})$ are artificially modified such that SOC and elastic scattering

amplitudes from ion-core planes are selectively switched off. SOC in the state $\psi_i^{\sigma_i}(\boldsymbol{x})$ is switched off by replacing its fully relativistic calculation by a scalar relativistic one.

To specify the elastic scattering amplitude modifications, we recall a key ingredient of relativistic layer KKR theory (for details, see e.g. chapter 4.3.5 in [14]), the scattering by a single atomic layer (inside the crystal) with lattice periodicity parallel to the surface. The wave field incident on this layer from the surface side (bulk side) is defined by plane-wave-expansion spinor amplitudes u_g^+ (u_g^-), where g enumerates the surface reciprocal-lattice vectors (with $g = 0$ corresponding to $\boldsymbol{g} = (0, 0)$). The scattered wave field on the surface side (bulk side) is described by amplitudes v_g^- (v_g^+), The incoming field is transformed into the outgoing one by the S-matrix according to

$$v_g^\sigma = \sum_{\sigma' g'} M_{gg'}^{\sigma\sigma'} u_{g'}^{\sigma'} \tag{5}$$

where the S-matrix elements $M_{gg'}^{\sigma\sigma'}$ are themselves 2×2 spin matrices. The $M_{gg'}^{++}$ ($M_{gg'}^{--}$) thus describe transmission through the layer from its surface side to its bulk side (from its bulk to its surface side), and the $M_{gg'}^{-+}$ ($M_{gg'}^{+-}$) represent reflection at the surface side (bulk side).

In the present work we denote $M_{gg'}^{++}$ by $T_{gg'}^{(i)}$ and $M_{gg'}^{-+}$ by $R_{gg'}^{(i)}$, where the index $i = 1, 3, 4$ distinguishes between the primary electron state and the two ejected electron states. For the ith state, elastic back reflection towards the surface can thus be completely switched off by setting $R_{gg'}^{(i)} = 0$ for all surface-parallel atomic layers. We do this individually for one state at a time and use the resulting wave functions $\psi_i^{\sigma_i}(\boldsymbol{x})$ for calculating the (e, 2e) cross section according to equations (1), (2).

2.3. Application to W(001)

With a view to performing numerical calculations for W(001), we make the following specifications. The surface geometry is that of a truncated bulk crystal but with an inward relaxation of the topmost atomic layer by 7%, as was determined by SPLEED calculations and measurements [13].

The optical potential for the occupied states is a self-consistent LMTO potential cast into the muffin-tin form. For the continuum states it is augmented by an energy-dependent imaginary inner potential part and a continuous surface potential barrier with image asymptotics.

As for the screened electron–electron interaction (equation (3)), a realistic calculation of the dielectric function $\varepsilon(\boldsymbol{x}, \boldsymbol{x}'')$ for W(001), i.e. a highly inhomogeneous electron gas, is well beyond the scope of the present work. Instead, we resort to the Thomas–Fermi approximation

$$V(\boldsymbol{x}, \boldsymbol{x}') = \frac{\mathrm{e}^{-|\boldsymbol{x}-\boldsymbol{x}'|/\lambda}}{|\boldsymbol{x} - \boldsymbol{x}'|}. \tag{6}$$

To obtain a physically reasonable estimate of the screening length λ in equation (6), we start from the Thomas–Fermi expression (at $T = 0$)

$$\lambda = (4\pi e^2 N(E_F))^{(-1/2)} \tag{7}$$

where $N(E_F)$ is the total density of states at the Fermi energy E_F (cf. e.g. chapter 17 of [20]). Rather than approximating $N(E_F)$ by a non-interacting homogeneous electron gas value, as is frequently done, we take it from our self-consistent LMTO calculation. We thus obtain the value $\lambda = 0.48$ Å.

The above simple screening approximation appears acceptable for the present purpose for the following reasons: (a) the spin-averaged (e, 2e) intensities which were calculated with it are in rather good agreement with experimental data [9]; (b) physically reasonable departures of λ

from the above value are found to change our calculated spin-dependent intensities $I^{\pm}(E_3, E_4)$ for each energy pair (E_3, E_4) only by a nearly constant factor; hence they leave the spin asymmetry A (cf. equation (4)), which is the main focus of this work, unchanged.

With regard to the reaction geometry, we focus on the two coplanar set-ups shown in figure 1: (a) normal incidence and symmetric detector positions; (b) grazing incidence and non-symmetric detector positions. The x, z-plane is chosen parallel to the W(010) plane and hence is a mirror-symmetry plane of the crystal. Furthermore, it is a mirror plane of the complete set-up if the primary beam is unpolarized or has its spin-polarization vector $\boldsymbol{P}_1$ parallel to the y-axis. If $\boldsymbol{P}_1$ is parallel to the x, z-plane, the mirror operation M_{xz} transforms it into $-\boldsymbol{P}_1$ while leaving the remainder of the set-up unchanged. In particular, the intensity $I^{+}(E_3, E_4)$, which is a scalar quantity, is invariant under M_{xz}. This implies that $I^{+}(E_3, E_4) = I^{-}(E_3, E_4)$, i.e. the asymmetry $A(E_3, E_4)$ (equation (4)) is identically zero in this case. In contrast, for $\boldsymbol{P}_1$ parallel to $\boldsymbol{y}$, i.e. normal to the reaction plane, there is no general connection between I^{+} and I^{-}. One can thus in general expect a non-vanishing asymmetry A. We recall that the above findings are analogous to what is well known in spin-polarized LEED (SPLEED) (cf. e.g. [14]). For our numerical investigations of spin-polarized (e, 2e) spectroscopy, we therefore choose the primary electron spin alignment along $\boldsymbol{y}$.

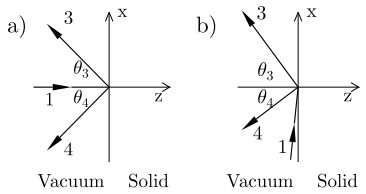

Figure 1. A sketch of the two coplanar (e, 2e) geometries used in the present calculations: (a) $\vartheta_1 = 0$ (normal incidence) and $\vartheta_3 = \vartheta_4 = 40^\circ$; (b) $\vartheta_1 = 88^\circ$ (grazing incidence), $\vartheta_3 = 33^\circ$, and $\vartheta_4 = 47^\circ$. The primary electron beam has spin-polarization vector $\boldsymbol{P}_1 = (0, \pm 1, 0)$, i.e. normal to the reaction plane (x, z). The spins of the two outgoing electrons 3 and 4 are not resolved. The x, z-plane is parallel to the (010) plane of the crystal.

3. Numerical results for W(001)

In the following we present and discuss numerical results of spin-polarized (e, 2e) spectroscopy applied to W(001) for the two coplanar geometries shown in figure 1, with the spin of the primary electrons aligned along $\pm\boldsymbol{y}$, i.e. normal to the reaction plane.

3.1. Results for normal incidence

For the geometry shown in figure 1(a), typical results, obtained for primary beam energy 24.6 eV, are displayed in figure 2 as grey-scale contour plots in the E_3, E_4-plane. In these plots, the counter-diagonal† line with outgoing electron pair energies $E_3 + E_4 = 20$ eV corresponds, from energy conservation, to valence electrons with energy $E_2 = E_F = -\Phi$, where $\Phi = 4.6$ eV is the work function of W(001). The (dashed) diagonal line, with equal pair energies $E_3 = E_4$, may be viewed as an E_2-axis. In the two top panels of figure 2, the intensities I^{+} and I^{-} for spin-up and spin-down primary electrons (cf. equation (1)), respectively, are seen to be largest for E_2 in the range between E_F and $E_F - 2.5$ eV, almost zero in the next 2 eV

† By 'counter-diagonals' we designate lines of constant total pair energy $E_3 + E_4$ in our $I(E_3, E_4)$ contour plots.

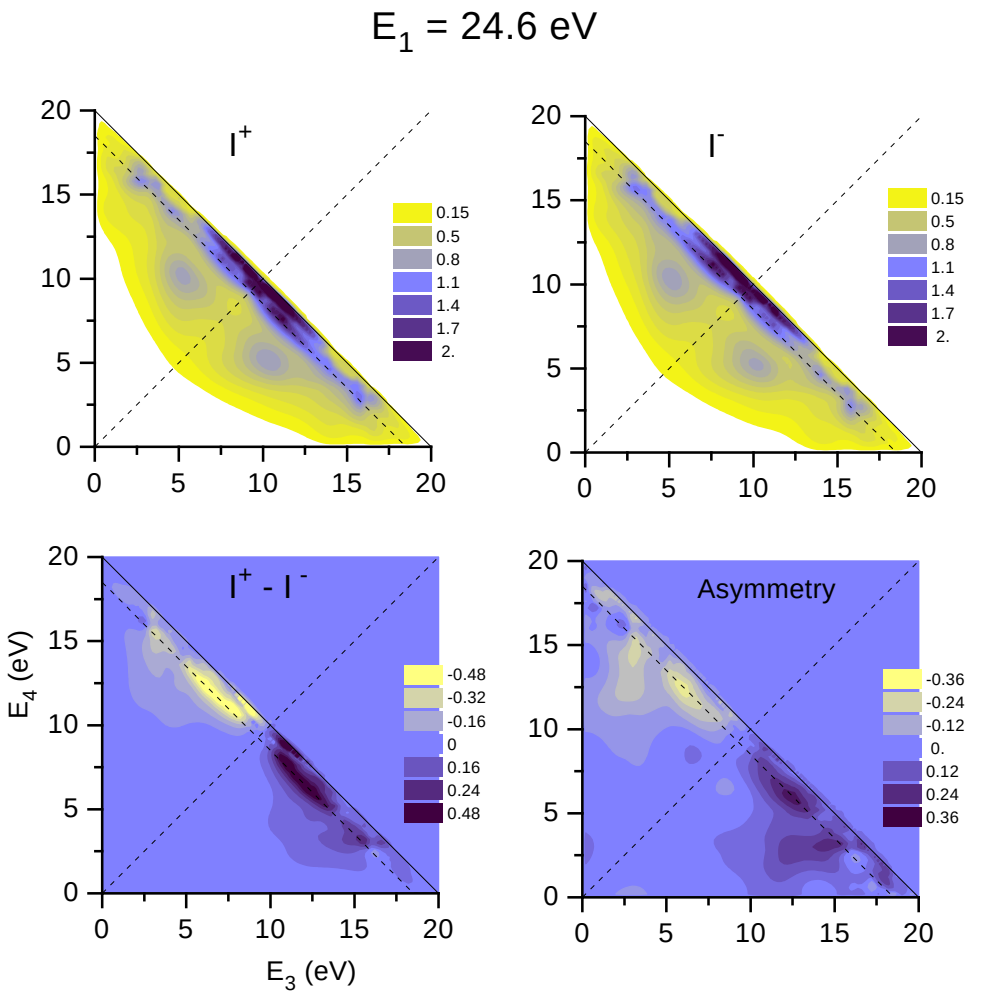

Figure 2. Spin-polarized (e, 2e) results for W(001) in the coplanar normal-incidence geometry of figure 1(a), for primary electron energy $E_1 = 24.6$ eV. The grey-scale contour plots in the E_3, E_4-plane show: (top left) the cross section $I^+(E_3, E_4)$ obtained for primary electron spin up (along $+\boldsymbol{y}$); (top right) the cross section $I^-(E_3, E_4)$ for primary electron spin down (along $-\boldsymbol{y}$); (bottom left) the difference $D = I^+ - I^-$; and (bottom right) the asymmetry $A = (I^+ - I^-)/(I^+ + I^-)$. Along the dashed diagonal line in each panel, the two outgoing electrons have equal energies, $E_3 = E_4$. The solid counter-diagonal line $E_3 + E_4 = 20$ eV and the dashed one $E_3 + E_4 = 18.5$ eV correspond to collisions with valence electrons at the Fermi energy and -1.5 eV below it, respectively. We used up to 20 different shades, a selection of which are shown in the 'grey-scale bar' inserted into each panel; each of these shadings represents an interval around the indicated value. The intensities are given in arbitrary units; the asymmetry is by definition normalized to 1, with ± 1 corresponding to $\pm 100\%$.

range, and again significant between -4.5 and -6 eV. We recall that this finding is similar to the results for unpolarized primary electrons at lower energies, and is in line with the $\boldsymbol{k}^{\parallel}$-resolved density of valence states [9]. I^+ and I^- appear rather similar, but closer inspection reveals significant differences, which become more apparent in the difference and asymmetry plots shown in the two lower panels of figure 2.

The contour plots exhibit an interesting symmetry property. Reflection at the $E_3 = E_4$ diagonal, i.e. interchanging E_3 and E_4, transforms I^+ into I^- and hence A into $-A$. This is readily understood from the geometry shown in figure 1(a). Reflection at the y, z-plane reverses the spin of the primary electron and interchanges the outgoing electrons 3 and 4, which implies that $I^+(E_3, E_4) = I^-(E_4, E_3)$.

The results in the contour plots in figure 2 can be displayed in a more quantitative way by means of so-called energy-sharing curves $I^{\pm}(E_3 - E_4)$, which represent $I^{\pm}(E_3, E_4)$ along counter-diagonal lines of constant $E_3 + E_4$. In figure 3 we show a selection of such energy-sharing curves, which are characterized by the corresponding valence electron energies -0.5 to -2.0 eV below E_F. It is obvious that $I^{\pm}(E_3 - E_4)$ and $A(E_3 - E_4)$ exhibit the reflection behaviour which we discussed for the contour plots in figure 3. Most importantly for our present work, I^+ and I^- differ appreciably from each other, and the corresponding asymmetry profiles $A(E_3 - E_4)$, which are richly structured, attain maxima up to 25%.

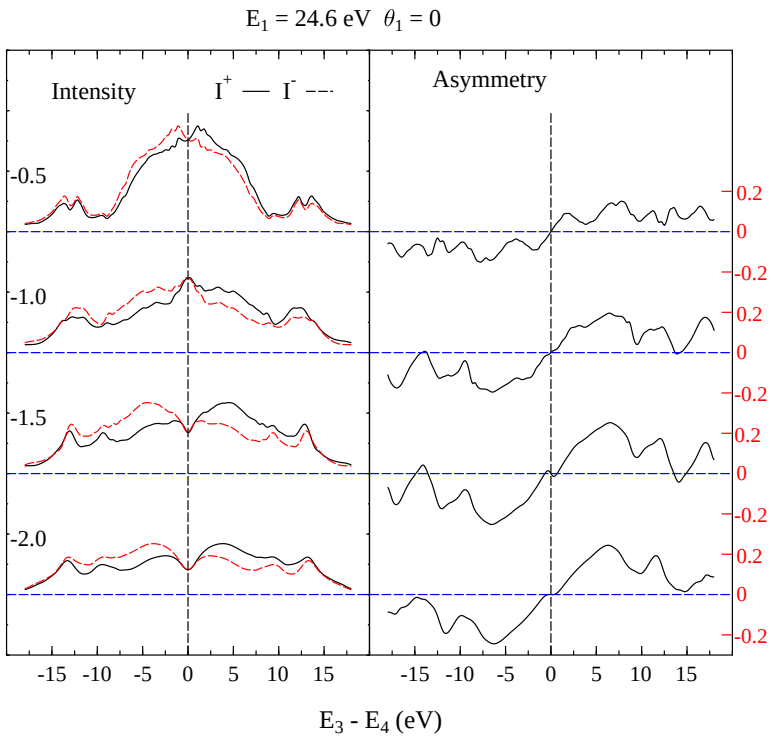

Figure 3. Energy-sharing curves of intensities I^+ and I^- (solid and dashed lines in the left-hand half) and asymmetry A (solid lines in the right-hand half) corresponding to the contour plots in figure 2 along a set of counter-diagonal lines $E_3 + E_4 = 20\,\text{eV} + x$ eV, with values of x as indicated in the individual panels; x corresponds to the valence electron energy relative to the Fermi energy. The intensities are in the same arbitrary units as in figure 2.

To elucidate the physical mechanisms responsible for prominent features in the $I^{\pm}(E_3 - E_4)$ curves and their asymmetries, we focus on the results for valence electron energy -1.5 eV, and present in figure 4 corresponding results with SOC and elastic layer scattering matrices in the four one-electron states selectively switched off as described in section 2.2. We first note that the line shapes of the 'fully calculated' I^+ and of I^- (figure 4(a)) change fairly little if SOC is switched off in the primary electron state (figure 4(b)) or in the ejected electron

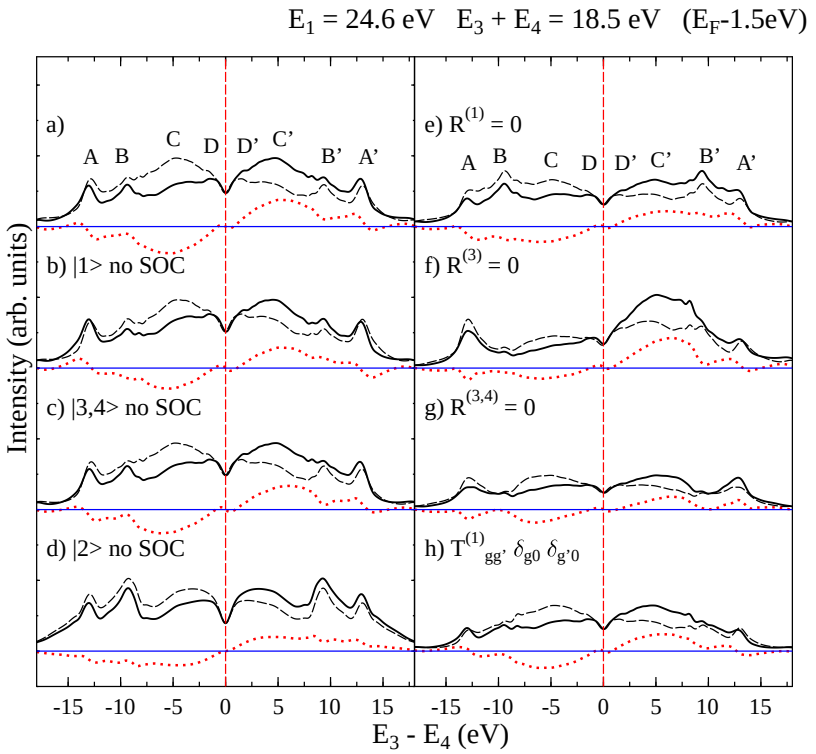

Figure 4. Energy-sharing curves for I^+ (solid lines), I^- (dashed lines), and the difference $I^+ - I^-$ (dotted lines) in the normal-incidence geometry (figure 1(a)) for $E_1 = 24.6$ eV and $E_3 + E_4 = 18.5$ eV (i.e. $E_2 = E_F - 1.5$ eV). Results of the 'complete calculation' (panel (a)) are compared with results of calculations in which spin–orbit coupling and elastic layer reflection matrices $R^{(i)}$ in the four one-electron states (1: primary electron; 2: valence electron; 3 and 4: outgoing electrons) were selectively switched off (cf. section 2.2) as indicated in panels (b) to (g); in panel (h), all elements of the layer transmission matrix $T^{(1)}$ of the primary electron have been set to zero except the first diagonal element.

states (figure 4(c)), but are appreciably modified if there is no SOC in the valence state. The latter appears plausible from the well-known substantial influence of SOC on the valence band structure of W [16, 17]. The comparatively smaller influence of SOC in the excited states can be understood in the following way. Whilst the valence states have predominant d character ($l = 2$), the excited-state bands which can couple to the vacuum to form the LEED states are mostly sp-like ($l = 0, 1$) (cf. e.g. [21]), and SOC is overall stronger for the occupied valence d states than for the unoccupied sp states.

In order to identify the scattering paths which are mainly responsible for the existence of individual intensity peaks and for their asymmetry, a selection of scattering paths, which involve various combinations of the plane-wave expansion parts of the primary electron state and of the outgoing electron states, are illustrated by symbolic diagrams in figure 5. Formally, these diagrams correspond to additive terms in a scattering path expansion of the direct and exchange scattering amplitudes f and g (cf. equation (2)). Because of the absolute square in equation (1) it is clear that the magnitude of a particular cross-section feature is in general not equal to the sum over partial intensities (obtained from the f- and g-parts symbolized by the diagrams), but in many cases this turns out to hold approximately.

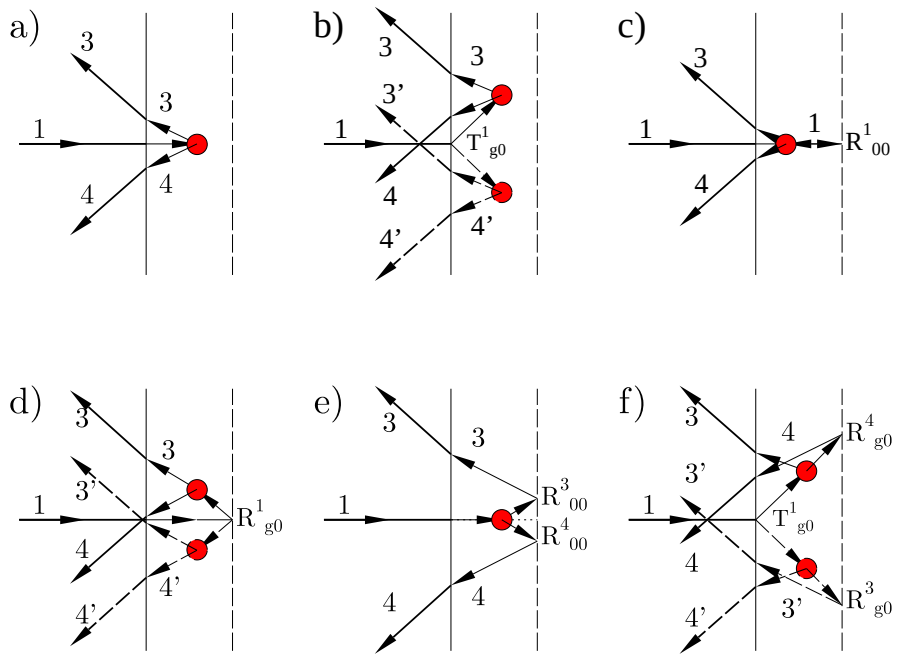

Figure 5. Symbolic diagrams of typical scattering paths in the (e, 2e) process for normal incidence of the primary electron (labelled 1) and polar angles of 40° of the detected electrons (3 and 4). The vertical thin solid line indicates the surface. The filled circle symbolizes the collision with the valence electron. The vertical thin dashed lines stand for the atomic planes, and the $R^{i}_{gg'}$ on their right-hand sides are the elastic reflection matrix elements, which are relevant in the individual diagrams. In diagrams (d) and (f), the thick solid and dashed lines depict two different paths, which are related to each other by symmetry. The refraction angle of electron 3 at the surface has been drawn equal to that of electron 4, which is actually the case only for $E_3 = E_4$. For $E_3 \neq E_4$, the diagrams are topologically equivalent to the ones shown, but—due to the energy dependence of refraction at the surface—the internal angles of electron 3 are different from those of electron 4.

We now interpret the individual intensity peaks in figure 4(a) and deduce the relevant scattering paths by comparing each peak with its switch-off counterparts in panels (b)–(h) of figure 4.

For peak A, we thus find that the most important scattering paths are those symbolized in figure 5(b) and figure 5(f), which involve off-diagonal elements $T^{(1)}_{g0}$ of the transmission matrix, and that its asymmetry is produced by SOC in state 1. In the following, we provide a more detailed analysis of peak A and show how these results have been obtained. From panels (a)–(d) of figure 4 it is evident that the asymmetry of peak A and that of its counterpart A′ arise purely from spin–orbit coupling in state 1. This implies, because of normal incidence, that it must be associated with off-diagonal elements $T^{(1)}_{g0}$ of the transmission matrix or $R^{(1)}_{g0}$ of the reflection matrix, where the index g refers to a two-dimensional reciprocal-lattice vector $\boldsymbol{g}$. Because of the low energy and of the coplanar geometry, the most relevant $\boldsymbol{g}$ are $(1, 0)2\pi/a_0$ and $(-1, 0)2\pi/a_0$. Paths involving $R^{(1)}_{g0}$, which are depicted in figure 5(d), are however ruled out by the persistence of the asymmetry of peak A in figure 4(e), where $R^{(1)} = 0$. On the other hand, peak A is strongly reduced and its asymmetry vanishes if the off-diagonal elements of $T^{(1)}$ are switched off (cf. figure 4(h)). This pinpoints the crucial role of the above-mentioned

$T_{g0}^{(1)}$. Possible scattering paths are therefore the ones shown in figure 5(b) and figure 5(f) plus a pair of paths like those in figure 5(f), except that now both electron 3 and electron 4 undergo a reflection before leaving the crystal. The existence of a reduced peak A with substantial asymmetry in figure 4(g), where $R^{(3,4)} = 0$, implies that the direct-exit paths in figure 5(b) contribute significantly. Figure 4(f) points to the importance of the path with $R^{(4)}$ in figure 5(f). That the apparently equivalent path with $R^{(3)}$ is actually negligible can be understood from the large difference between the energies of two electrons: $E_3 = 2.75$ eV and $E_4 = 15.75$ eV. Therefore in general $R^{(3)} \neq R^{(4)}$. Since electron 3 is strongly refracted at the surface (becoming close to normal inside the crystal) and electron 4 only weakly so, the two path diagrams in figure 4(f) are in this case not mirror symmetrical with each other. This inequivalence is essential for the left–right asymmetry of $T_{g0}^{(1)}$ and $T_{-g0}^{(1)}$ to be able to produce a spin asymmetry of the (e, 2e) intensity. Contrasting with peak A, its counterpart A′ at $(E_3, E_4) = (15.75, 2.75)$ stems partly from the lower path in figure 5(f), which involves $R^{(3)}$, and is consequently reduced in figure 4(f).

Peaks B, C, and D in figure 4 can be interpreted along analogous lines. For peak B, figure 4(f) indicates that $R^{(3)}$ is important, and hence also the lower diagram in figure 5(f). The asymmetry of B is partly due to spin–orbit coupling in states 3 and 4, i.e. it is the usual SPLEED asymmetry for these states. This suggests that paths with direct transmission $T_{00}^{(1)}$ like the one in figure 4(e) can contribute significantly.

Peak C and its counterpart C′ originate mainly from the lower and the upper paths in figure 5(f) (and their $T_{00}^{(1)}$-analogues), respectively. But, as figure 4(e) indicates, paths with primary beam reflection $R^{(1)}$ like in figure 5(d) are also important. Since a large part of the spin asymmetry of peak C persists if there is no SOC in states 1, 3, and 4 (cf. figure 4(b), 4(c)), it must be produced by SOC in the valence state. An explanation of how this happens is provided by our construction of the valence states $\psi_2^{\sigma_2}(\boldsymbol{x})$ (cf. section 2.1): each one involves a Bloch wave propagating off-normally (because $\boldsymbol{k}_2^{\parallel} \neq 0$ if $E_3 \neq E_4$) towards the surface, at which it is reflected into Bloch waves going into the crystal. This process may be viewed as a kind of spin-polarized LEED from inside. Because of SOC, the reflection amplitudes and therefore the amplitudes of the ingoing Bloch waves are in general different for $\sigma_2 = +$ and $\sigma_2 = -$. Consequently, the pairs of scattering amplitudes (cf. equation (2)) $f_{\sigma_1,n\sigma_2,\sigma_3,\sigma_4}$ with $\sigma_2 = \pm$ are different for $\sigma_1 = +$ and $\sigma_1 = -$. The same holds for the exchange scattering amplitudes g. The σ_1-dependence survives the σ_2-summation in equation (1) and therefore extends to the intensities I^{σ_1}.

In order to assess the sensitivity of (e, 2e) spectroscopy to the surface structure, we performed additional calculations, in which the reduction of the topmost interlayer spacing was varied from the value -7% (determined by SPLEED analysis in [13]). Some typical spin-dependent intensity and asymmetry results are shown as energy-sharing curves in figure 6. Going from 0 to -10% relaxation, the spectra change substantially in overall height and in line shape. The broad intensity peak C is seen to grow more strongly than its neighbour B. In all of the panels, C is associated with a broad asymmetry feature, the magnitude of which decreases from close to 40% to the still sizable value of 20%. In contrast, the asymmetry of B is fairly small and changes only weakly. Such selective sensitivity of neighbouring features is known from SPLEED to be particularly useful for determining structure parameters by comparing calculated spectra with their experimental counterparts.

3.2. Results for grazing incidence

In figure 7 we show contour plots calculated for the grazing-incidence geometry of figure 1(b), with primary electrons of energy 20.6 eV spin polarized along $\pm\boldsymbol{y}$. In the two top panels, the

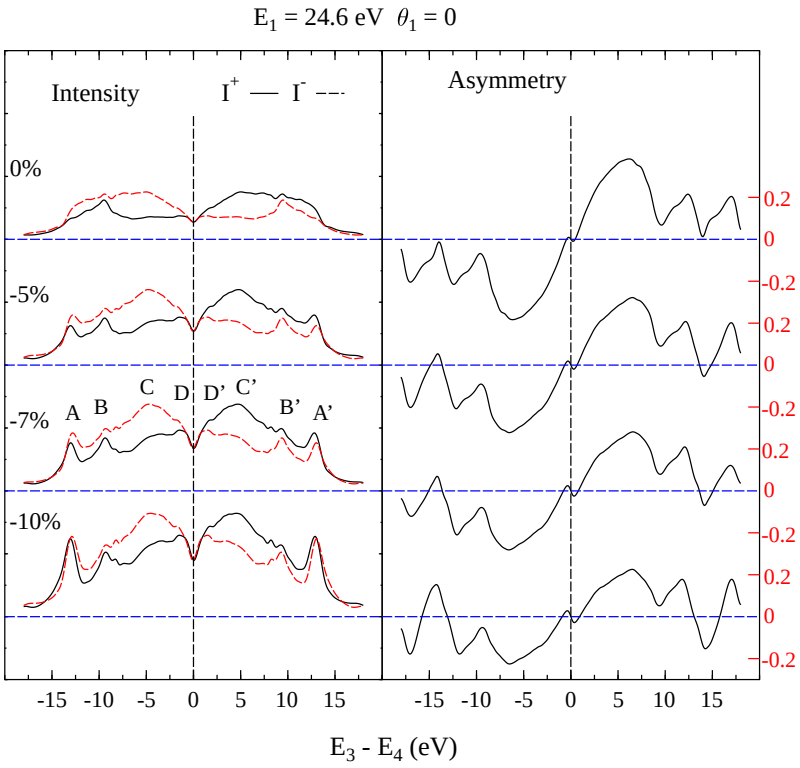

Figure 6. The influence of the inward surface relaxation of W(001) on the energy-sharing curves of intensities I^+ and I^- (solid and dashed lines in the left-hand half) and asymmetry A (solid lines in the right-hand half) in the normal-incidence geometry (figure 1(a)) for $E_1 = 24.6$ eV and $E_3 + E_4 = 18.5$ eV (i.e. $E_2 = E_F - 1.5$ eV). The percentage deviation of the topmost interlayer spacing from the bulk value is indicated in the respective panels.

intensities I^+ and I^- are seen to be largest for collisions with valence electrons of energy E_2 within a 2.5 eV range from the Fermi energy E_F. I^+ and I^- are substantially different around $(E_3, E_4) = (4.5,\ 11.5)$, with corresponding sizable peaks in the difference and asymmetry plots, which are shown in the two bottom panels of figure 7. In contrast to the normal-incidence results in figure 2, there is no mirror symmetry with respect to the $E_3 = E_4$ diagonal line. This is easily understood from the fact that in an oblique-incidence geometry there is no spatial transformation which only interchanges the two detection directions and reverses the primary electron spin.

From the results shown in the contour plots of figure 7, we present in figure 8 a set of energy-sharing curves, which are characterized by valence electron energies -0.5 to -2.0 eV below E_F. For $E_3 > E_4$ the intensity line shapes are fairly similar and the peak around 10 eV has a spin asymmetry of about -10%. For $E_3 < E_4$, the sharing curve for I^+ with $E_2 = -0.5$ eV has a particularly strong peak around -7 eV, with an asymmetry of 30%.

We therefore choose the sharing curves with $E_2 = -0.5$ eV for a more detailed investigation analogous to the one performed above in the normal-incidence case. Panels (a)–(d) in figure 9 demonstrate the effects of switching off spin–orbit coupling. Comparison of panels (a)–(c) reveals that SOC in states 1, 3, and 4 has no noticeable influence on the spectra, except for the disappearance of the asymmetry of peak C, which is jointly produced

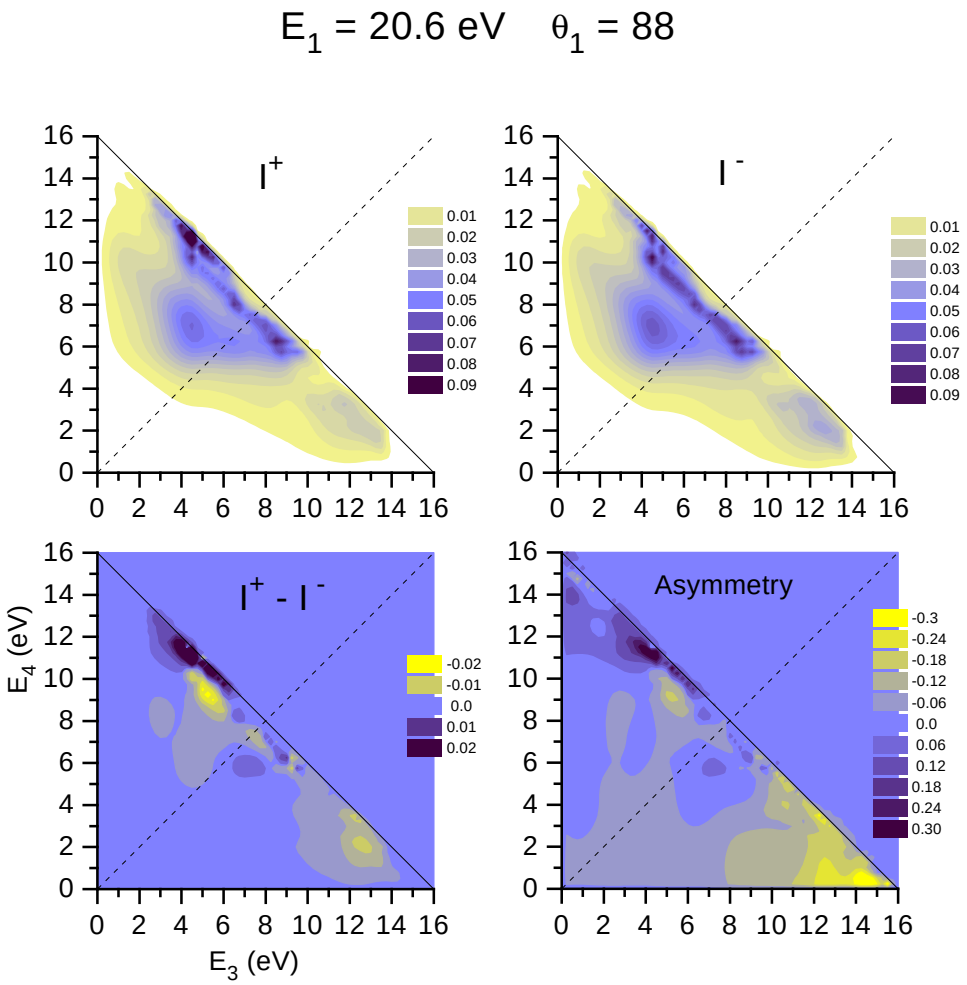

Figure 7. Spin-polarized (e, 2e) contour plots for W(001) as in figure 2, but for the grazing-incidence ($\vartheta_1 = 88^\circ$) geometry sketched in figure 1(b), with primary electron energy $E_1 = 20.6$ eV. The solid counter-diagonal line $E_3 + E_4 = 16$ eV corresponds to collisions with valence electrons at the Fermi energy.

by SOC in these states. If however the valence electron state 2 is calculated without SOC, the entire spectral shape changes drastically (figure 9(d)). In particular the strongly spin-dependent dominant peak A almost vanishes. Its large asymmetry is seen to be almost entirely due to SOC in the valence state. For an explanation of the underlying mechanism we refer the reader to the penultimate paragraph of section 3.1.

Insight into the scattering paths, which are relevant for individual intensity and asymmetry features, is gained from the energy-sharing curves in panels (e)–(h) of figure 9, which were calculated with selected elastic layer reflection and transmission amplitudes switched off. The dominant peak A is seen to be somewhat reduced if $R^{(3)} = 0$, and practically vanishes for $R^{(4)} = 0$. Additional calculations, in which only $R^{(4)}_{00}$ was switched off, did not however produce any change of peak A. This implies that peak A strongly relies on non-specular reflection matrix elements $R^{(4)}_{g0}$. We identify the most relevant reciprocal-lattice vector labelled

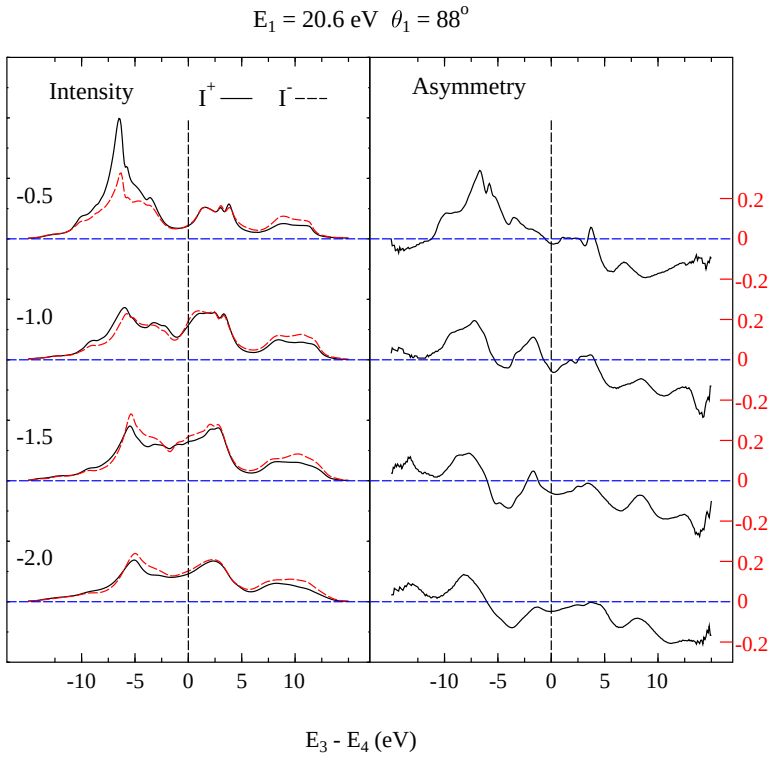

Figure 8. Energy-sharing curves of intensities I^+ and I^- (solid and dashed lines in the left-hand half) and asymmetry A (solid lines in the right-hand half) corresponding to the contour plots in figure 7, taken along a set of counter-diagonal lines $E_3 + E_4 = 16$ eV + x eV, with values of x as indicated in the individual panels; x corresponds to the valence electron energy relative to the Fermi energy.

by g as $\boldsymbol{g} = (-1, 0)$, since the other $\boldsymbol{g}$ in the reaction plane belong to internally evanescent beams. The corresponding scattering path diagram is shown in figure 10(a), in which the collision is followed by direct emission of electron 3 and emission of electron 4 via non-specular reflection. A minor contribution can be ascribed to the path shown in figure 10(b), which involves reflection of both electron 3 and electron 4.

For the double peaks B and C, the reductions seen in figure 9(f) and figure 9(g) mainly point to scattering paths like the one shown in figure 10(b).

If reflection $R^{(1)}$ or non-specular transmission $T^{(1)}_{g0}$ of the primary electron is switched off, all of the peaks are significantly enhanced (cf. figures 9(e) and 9(h)). While surprising at first glance, this can easily be understood as a consequence of adding up the partial scattering amplitudes associated with different symbolic diagrams (for details, see above in the context of figure 5). We conclude that the path shown in figure 10(c) plays an important role. This is particularly interesting for peak C, the asymmetry of which vanishes in figures 9(e) and 9(h), and thus can be traced back to this path. From SPLEED knowledge it is evident that the amplitude of beam 1 'just before the collision' should depend on the spin of the primary electron and so consequently should the (partial) scattering amplitude.

Energy-sharing curves for a sequence of different primary electron energies E_1 are shown in figure 11. From the almost spin-independent near-centre peak at $E_1 = 14.6$ eV a

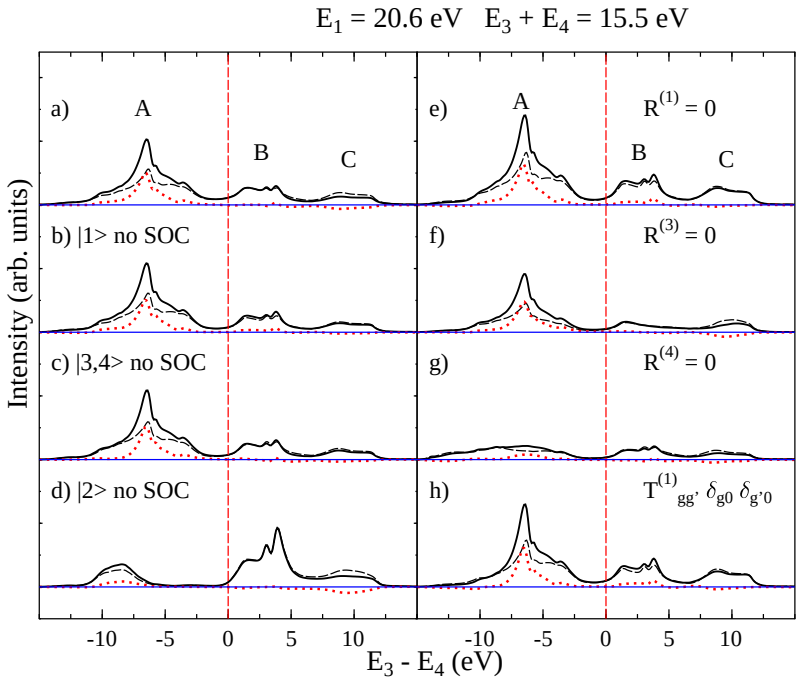

Figure 9. Energy-sharing curves for I^+ (solid lines), I^- (dashed lines), and the difference $I^+ - I^-$ (dotted lines) in the grazing-incidence geometry (figure 1(b)) for $E_1 = 20.6$ eV and $E_3 + E_4 = 15.5$ eV (i.e. $E_2 = E_F - 0.5$ eV): results of the 'complete calculation' (panel (a)) are compared with results of calculations in which spin–orbit coupling and elastic scattering amplitudes in the four one-electron states (1: primary electron; 2: valence electron; 3 and 4: outgoing electrons) were selectively switched off as indicated in panels (b) to (h).

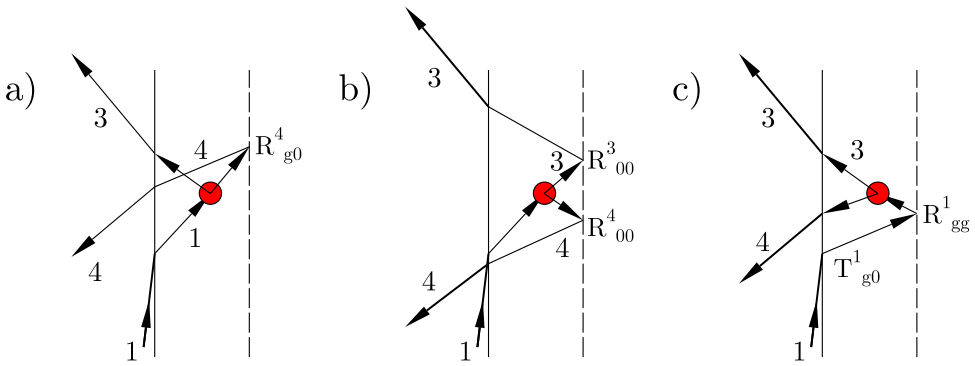

Figure 10. Symbolic diagrams of three important scattering paths in the (e, 2e) process for grazing incidence of the primary electron (labelled 1) and polar angles 33° and 47° of the detected electrons 3 and 4, respectively. The symbols used are the same as in figure 5.

substantially spin-dependent peak is seen to have split off towards the left at $E_1 = 16.6$ eV. With increasing E_1, it disperses to the left and, while its size decreases, the asymmetry associated with it increases up to about 30% at $E_1 = 22.6$ eV. It should therefore be easily observable in a

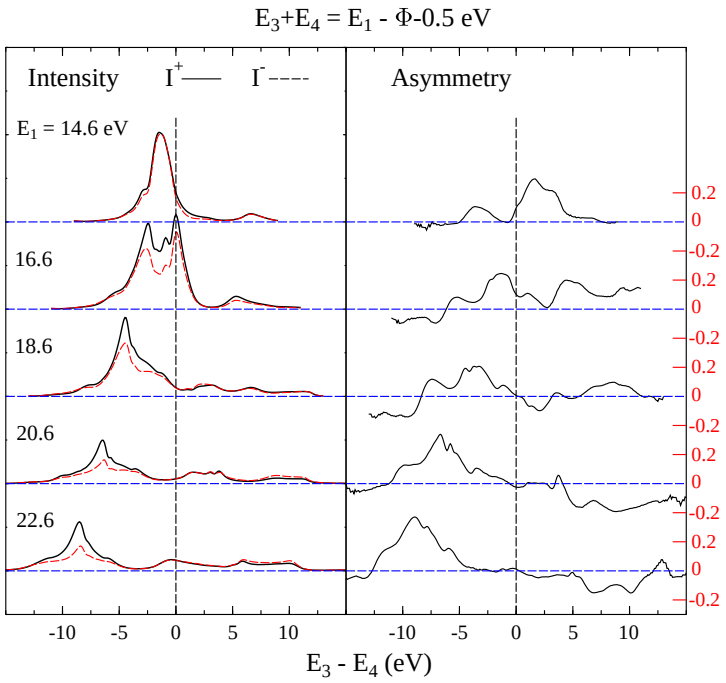

Figure 11. Energy-sharing curves of intensities $I^{\pm}$ and asymmetry A for the grazing-incidence geometry (cf. figure 1(b)) and various primary beam energies E_1 as indicated in the panels. The detected electrons with energy sum $E_3 + E_4 = E_1 - \Phi - 0.5$ eV originate from collisions with valence electrons of energy 0.5 eV below the Fermi level.

spin-polarized (e, 2e) experiment. Its asymmetry, as deduced above in detail for $E_1 = 20.6$ eV, stems almost entirely from SOC in the valence state (at energy -0.5 eV below E_F).

4. Conclusions

Our numerical calculations for W(001) predict that the low-energy (e, 2e) scattering cross section depends significantly on the spin of the primary electron. This spin asymmetry reaches values up to 30% in conjunction with strong intensity. It is therefore easily within reach of present-day experimental capabilities.

The physical origin of the spin asymmetry is spin–orbit coupling (SOC) in at least one of the participating one-electron states. Calculations in which SOC was selectively switched off indicate that in some cases the asymmetry arises mainly from the primary electron state, which is the usual SPLEED state. For the majority of peak asymmetries, however, SOC in the valence state is partly or fully responsible. The underlying mechanism can be pictorially understood as SPLEED at energies below E_F, with an unpolarized Bloch electron beam impinging from inside the crystal onto the surface, and the process of collision with the spin-polarized primary electron acting as a spin detector for the back-diffracted Bloch electrons. Since the surface is thus vital for the very existence of the asymmetry A of the (e, 2e) scattering cross section, A responds sensitively to changes in the surface region and promises to be a useful tool for studying geometrical and electronic properties of surfaces and thin films.

An analysis of the scattering paths revealed an important role of elastic reflection of the

primary electron and of one or both outgoing electrons at the ion-core planes.

Our present results for a non-magnetic system have implications for spin-polarized (e, 2e) spectroscopy applied to ferromagnetic systems. Although for these the exchange interaction can generally be expected to be the main source of an observed spin asymmetry, SOC will also be of importance and will have to be taken into account in calculations and in the interpretation of experimental data.

References

[1] Whelan C T and Walters H R J (ed) 1997 *Electron Coincidence Studies of Electron and Photon Impact Ionization* (New York: Plenum)
[2] Canney S A, Vos M, Kheifets A S, Clisby N, McCarthy I E and Weigold E 1997 *J. Phys.: Condens. Matter* **9** 1931
[3] Vos M, Fang Z, Canney S A, Kheifets A S, McCarthy I E and Weigold E 1997 *Phys. Rev.* B **56** 963
[4] Artamonov O M, Samarin S N and Kirschner J 1995 *Phys. Rev.* B **51** 2491
[5] Kirschner J, Artamonov O M and Samarin S N 1995 *Phys. Rev. Lett.* **75** 2424
[6] Artamonov O M, Samarin S N and Kirschner J 1997 *Appl. Phys.* A **65** 535
[7] Iacobucci S, Marassi L, Camilloni R, Nannarone S and Stefani G 1995 *Phys. Rev.* B **51** 10 525
[8] Gollisch H, Meinert D, Xiao Yi and Feder R 1997 *Solid State Commun.* **102** 317
[9] Feder R, Gollisch H, Meinert D, Scheunemann T, Artamonov O M, Samarin S and Kirschner J 1998 *Phys. Rev.* B **58** 16 418
[10] Berakdar J and Das M P 1997 *Phys. Rev.* A **56** 1403
[11] Berakdar J, Samarin S N, Herrmann R and Kirschner J 1998 *Phys. Rev. Lett.* **81** 3535
[12] Kheifets A S, Iacobucci S, Ruocco A, Camilloni R and Stefani G 1998 *Phys. Rev.* B **57** 7380
[13] Feder R and Kirschner J 1981 *Surf. Sci.* **103** 75
[14] Feder R (ed) 1985 *Polarized Electrons in Surface Physics* (Singapore: World Scientific)
[15] Krewer J and Feder R 1989 *Solid State Commun.* **70** 205
[16] Christensen N E and Feuerbacher B 1974 *Phys. Rev.* B **10** 2349
[17] Feder R and Sturm K 1975 *Phys. Rev.* B **12** 537
[18] Henk J and Feder R 1994 *J. Phys.: Condens. Matter* **6** 1913
[19] Henk J and Feder R 1994 *Europhys. Lett.* **28** 609
[20] Ashcroft N W and Mermin N D 1976 *Solid State Physics* (New York: Holt-Saunders)
[21] Courths R, Loebus S, Halilov S, Scheunemann T, Gollisch H and Feder R 1999 *Phys. Rev.* B **60** 8055